nature nanotechnology

Supplementary information

https://doi.org/10.1038/s41565-026-02134-z

# Magnetic circular dichroism imaging of atomic-scale antiferromagnetic order at a buried interface

In the format provided by the authors and unedited

# Content

## Table of Contents

*Supplementary Note 1: Comparison of signal intensity using on-axis and off-axis setups* ..2

*Supplementary Note 2: Details of the simulation of EMCD signals in $DyFeO_3$* .....4

*Supplementary Note 3: Separation of EMCD signals from three orthogonal magnetization directions*.....6

*Supplementary Note 4: EMCD signals for Dy*.....8

*Supplementary Note 5: EMCD spectra across the $DyScO_3$-$SmFeO_3$ interface*.....10

*Supplementary Note 6: Dose dependence of EMCD signals*.....11

*Supplementary Note 7: Effect of beam misorientation on EMCD signals*.....13

*Supplementary Note 8: Simulation of the effect of a half–unit-cell offset shift on EMCD map measurement in $DyFeO_3$*.....15

*Supplementary Note 9: Alternative approach for the extraction of EMCD signals at the $SmFeO_3$-$DyScO_3$ interface*.....16

## Supplementary Note 1: Comparison of signal intensity using *on-axis* and *off-axis* setups

In the conventional EMCD geometry, with the sample magnetization oriented along the *z*-axis (parallel to the electron beam), the EMCD signals are always localized away from the transmitted beam, a characteristic observed under both three-beam and zone-axis conditions. In such configurations, an *off-axis* aperture (yellow rectangle marked in **Fig. S1a**) is typically used to selectively collect the EELS signals. In contrast, in our approach the magnetization is oriented along the *x*-axis or *y*-axis, resulting in EMCD signals that are concentrated around the transmitted beam. This configuration allows for the use of an *on-axis* aperture (yellow circle marked in **Fig. S1e**) for EELS signal collection. In order to make a quantitative comparison, we calculated the nonmagnetic (**Fig. S1b** and **S1f**) and magnetic (**Fig. S1c** and **S1g**) signal components across the entire unit cell of $DyFeO_3$ using the aperture configurations shown in **Fig. S1a** and **S1e**. The total EELS signal, obtained by summing the nonmagnetic and magnetic contributions, is shown in **Fig. S1d** and **S1h**. **Fig. S1i** presents the ratio of total signal intensities between the *on-axis* and *off-axis* configurations. Our *on-axis* approach yields a significantly stronger total signal - enhanced by more than an order of magnitude - compared to the conventional *off-axis* approach. This efficient collection of the localized magnetic signal directly leads to a marked improvement in SNR.

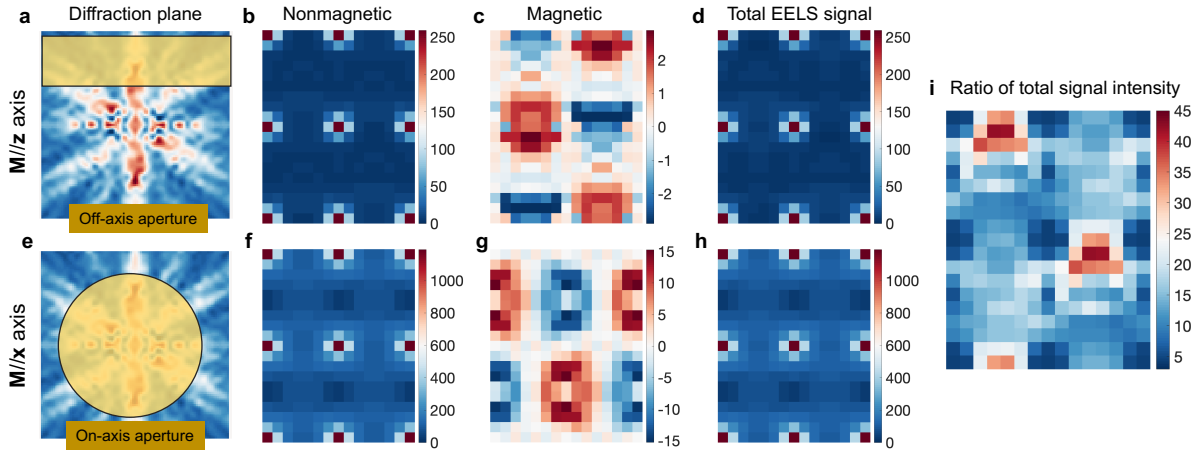


**Fig. S1 | Comparison of signal intensity using *on-axis* and *off-axis* apertures. a, e**, Schematic diagrams showing the positions of the EELS collection aperture for obtaining EMCD signals with the magnetization oriented along the *z* and *x* directions, respectively. **b-d**, Real-space maps of the simulated nonmagnetic, magnetic and total signals across the $DyFeO_3$ unit cell, assuming that the magnetization lies along the *z* direction (conventional EMCD diffraction geometry). **f-h**, As for **b-d**, but assuming that the magnetization lies along the *x* direction (this work). **i**, Ratio of total signal intensity between **d** and **h**.

## Supplementary Note 2: Details of the simulation of EMCD signals in $DyFeO_3$

The antiferromagnetic $DyFeO_3$ structure consists of two magnetic Fe sublattices with opposite spin orientations, i.e., $\overrightarrow{Fe}$ and $\overleftarrow{Fe}$. In our simulations, we take advantage of the ability to separately calculate the nonmagnetic and magnetic scattering contributions for each sublattice. Specifically, we define them as follows:

- $N(\overrightarrow{Fe})$ and $N(\overleftarrow{Fe})$ represent the nonmagnetic signals from the two Fe sublattices,
- $M(\overrightarrow{Fe})$ and $M(\overleftarrow{Fe})$ represent the magnetic signals from the two Fe sublattices.

The relative EMCD signals for each spin orientation are calculated as:

- $EMCD(\overrightarrow{Fe})$ in **Fig. S2** (upper panel): $M(\overrightarrow{Fe}) / (N(\overrightarrow{Fe}) + N(\overleftarrow{Fe}))$
- $EMCD(\overleftarrow{Fe})$ in **Fig. S2** (middle panel): $M(\overleftarrow{Fe}) / (N(\overrightarrow{Fe}) + N(\overleftarrow{Fe}))$

Because the two Fe sublattices have opposite spin orientations, the final EMCD signal ($EMCD(\overrightarrow{Fe})$ - $EMCD(\overleftarrow{Fe})$ ), which is shown in **Fig. S2** (lower panel), is obtained by subtracting the two spin-oriented signals:

$(M(\overrightarrow{Fe}) - M(\overleftarrow{Fe})) / (N(\overrightarrow{Fe}) + N(\overleftarrow{Fe}))$.

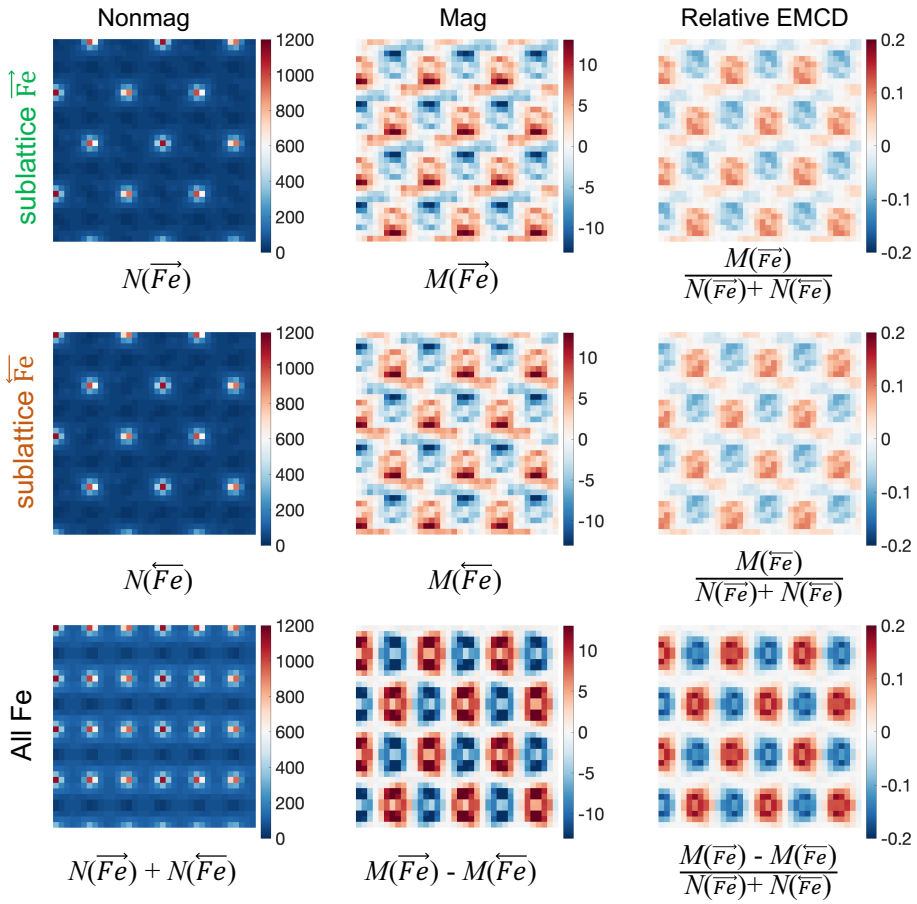


**Fig. S2 | Simulated real-space distributions of nonmagnetic, magnetic and relative EMCD signals.** Shown from left to right are simulated maps of nonmagnetic, magnetic and relative EMCD signals in real space. The upper, middle and lower panels correspond to Fe sublattice $\overrightarrow{Fe}$, Fe sublattice $\overleftarrow{Fe}$ and combined Fe lattice, respectively. Specifically, $N(\overrightarrow{Fe})$ and $N(\overleftarrow{Fe})$ denote nonmagnetic signals from the two Fe sublattices, while $M(\overrightarrow{Fe})$ and $M(\overleftarrow{Fe})$ represent their corresponding magnetic signals. The relative EMCD signals for each spin orientation are calculated as $EMCD(\overrightarrow{Fe}) = M(\overrightarrow{Fe}) / (N(\overrightarrow{Fe}) + N(\overleftarrow{Fe}))$ and $EMCD(\overleftarrow{Fe}) = M(\overleftarrow{Fe}) / (N(\overrightarrow{Fe}) + N(\overleftarrow{Fe}))$. Because the two Fe sublattices have opposite spin orientations, the total EMCD signal $EMCD(\overrightarrow{Fe})$ - $EMCD(\overleftarrow{Fe})$ is obtained as $(M(\overrightarrow{Fe}) - M(\overleftarrow{Fe})) / (N(\overrightarrow{Fe})+ N(\overleftarrow{Fe}))$, corresponding to the result shown in **Fig. 2b**.

## Supplementary Note 3: Separation of EMCD signals from three orthogonal magnetization directions

EMCD can be used to measure magnetic signals in three spatial directions on the nanometer scale, as EMCD signals arising from magnetization in the three Cartesian directions have distinct distributions in the diffraction plane[1–3]. This principle applies to both atomic-plane resolution and atomic-column resolution measurements. In the present study, we calculated the distribution of EMCD signals assuming that the magnetic vector is oriented along the *x*, *y* or *z* directions, as shown for $DyFeO_3$ in Extended Data Fig. 6a-d. By integrating the EMCD signals over the *on-axis* EELS aperture in the diffraction plane, one can visualize the real-space distribution of both nonmagnetic and magnetic EMCD signals for the three spin configurations in Extended Data Fig. 6e-h. The nonmagnetic signals remain unchanged, as they are independent of the spin configuration.

For spins oriented along the *x* axis, which represents a real magnetic configuration, the EMCD signals are localized between the Fe columns along the *y* direction, almost coinciding with the positions of the Dy columns. These signals exhibit an alternating pattern, with reversed signs. When the spins are oriented along the *y* axis, the EMCD signals are localized between the Fe columns along the *x* direction, showing a distinct distribution. For spins oriented along the *z* axis, the situation is similar to that for conventional EMCD, being sensitive only to magnetization along the electron beam direction (*z* axis). In this case, the EMCD signals exhibit an antisymmetric distribution in the diffraction plane, contributing to negligible or zero signals when using an *on-axis* EELS aperture, as shown in Extended Data Fig. 6h. Therefore, these signals can be neglected here.

The separation of EMCD signals from different directions is crucial for rigorously validating the feasibility of our method. For $DyFeO_3$, real-space maps of simulated EMCD signals across a unit cell are shown in **Fig. S3a-c**, assuming that the magnetization lies along the *x*, *y* and *z* directions, respectively. When the spins are oriented along the *x*-axis, the EMCD signals are localized primarily at the Dy sites (**Fig. S3a**). Corresponding line profiles (**Fig. S3d**) extracted from the blue rectangular region indicated in **Fig. S3a-c** reveal significant variations in EMCD intensity across atomic columns. For comparison, EMCD signals for the *y*- and *z*-oriented magnetizations are plotted in **Fig. S3d**. The *x*-component signal is more than an order of magnitude stronger at its characteristic Dy sites compared to the other two directions. Similarly, when the spins are oriented along the *y*-axis, the EMCD signals are localized between Fe sites (**Fig. S3b**). The line profiles in **Fig. S3e**, which are extracted from the black rectangular region

in **Fig. S3a-c**, confirm that the signals from the *x*- and *z*-oriented magnetizations are negligible compared to the signal from the *y*-direction. This quantitative analysis highlights the distinct spatial localization of the magnetic contributions and provides evidence for their separability at the atomic scale.

In our experiments, the EMCD signal maps shown in Fig. 2e-f are in good agreement with the results derived for spins along the *x* axis, as shown in Extended Data Fig. 6b and 6f. These results not only confirm the *x*-oriented spin configuration, but also demonstrate that atomic-column EMCD is able to resolve magnetic ordering without requiring prior magnetic information about the crystal, thereby showcasing its ability to resolve magnetic structure. Furthermore, to rule out EMCD signals arising from the spins oriented along the *y* axis, we summed the signals at the chiral+ and chiral- positions, as defined in Extended Data Fig. 6g for the *y*-oriented spin configuration. These chiral positions are also indicated in Extended Data Fig. 7 for the experimental ADF image. The extracted chiral+ and chiral- EELS signals, which are displayed in Extended Data Fig. 7 along with their difference, show negligible EMCD signals. This analysis further confirms that the spin orientation is along the *x* axis.

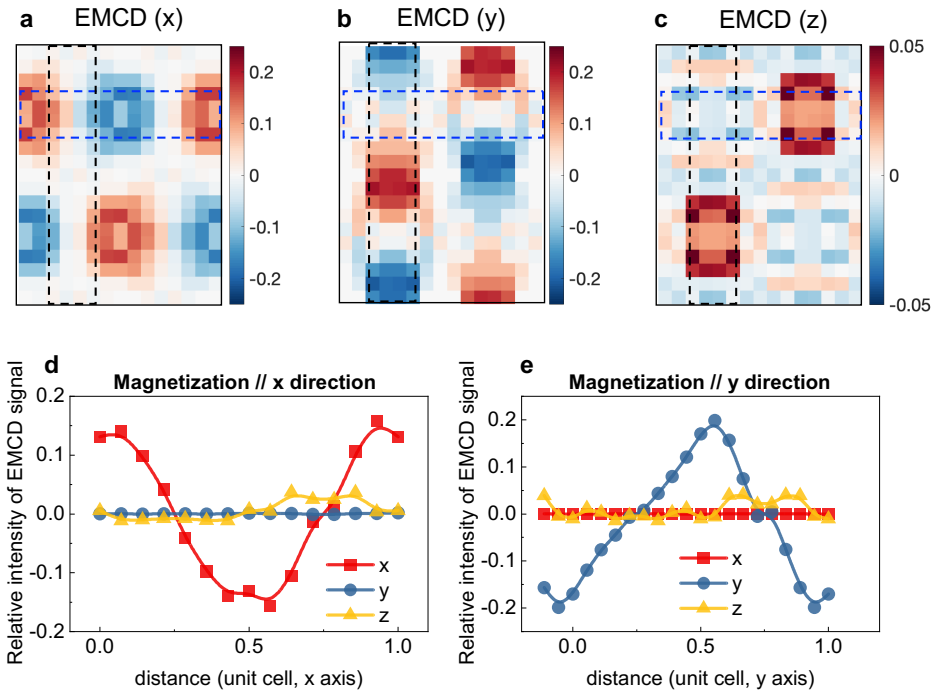


**Fig. S3 | Separation of EMCD signals along orthogonal magnetization directions. a-c,** Real-space maps of simulated EMCD signals across a unit cell of $DyFeO_3$, assuming magnetization along the *x*, *y* and *z* directions, respectively. **d,** Line profiles extracted from the blue rectangular region indicated in **a-c**. **e,** Line profiles extracted from the black rectangular region indicated in **a-c**.

## Supplementary Note 4: EMCD signals for Dy

In $DyFeO_3$, Dy possesses a large intrinsic magnetic moment, but its magnetic ordering temperature is well below room temperature. Consequently, no detectable EMCD signals are expected from Dy in the experiments. In order to verify this behavior, we performed additional analysis focused on the element Dy. In the magnetically-ordered state, the Dy moments are aligned along the *x*-axis and exhibit antiferromagnetic coupling between adjacent *c*-planes, as illustrated in **Fig. S4a**. In this configuration, the EMCD signal is expected to be localized between Dy atomic planes, similar to the case for $Fe_2O_3$ in **Fig. 3**. We integrated the EELS signals from regions between two Dy atomic planes, as shown schematically in **Fig. S4c**, which corresponds to the line intensity profiles extracted from the ADF image in **Fig. S4b**. The red and green regions indicate chiral+ and chiral- positions, respectively. The resulting chiral EELS signals and their difference (after background removal and post-edge normalization) for the Dy $M_{5,4}$ edges are presented in **Fig. S4d**. No statistically significant EMCD signal is observed for Dy. This null result contrasts with the strong and reproducible EMCD signals obtained from the Fe sublattice (**Fig. 2** in the main text), which remains magnetically ordered at room temperature.

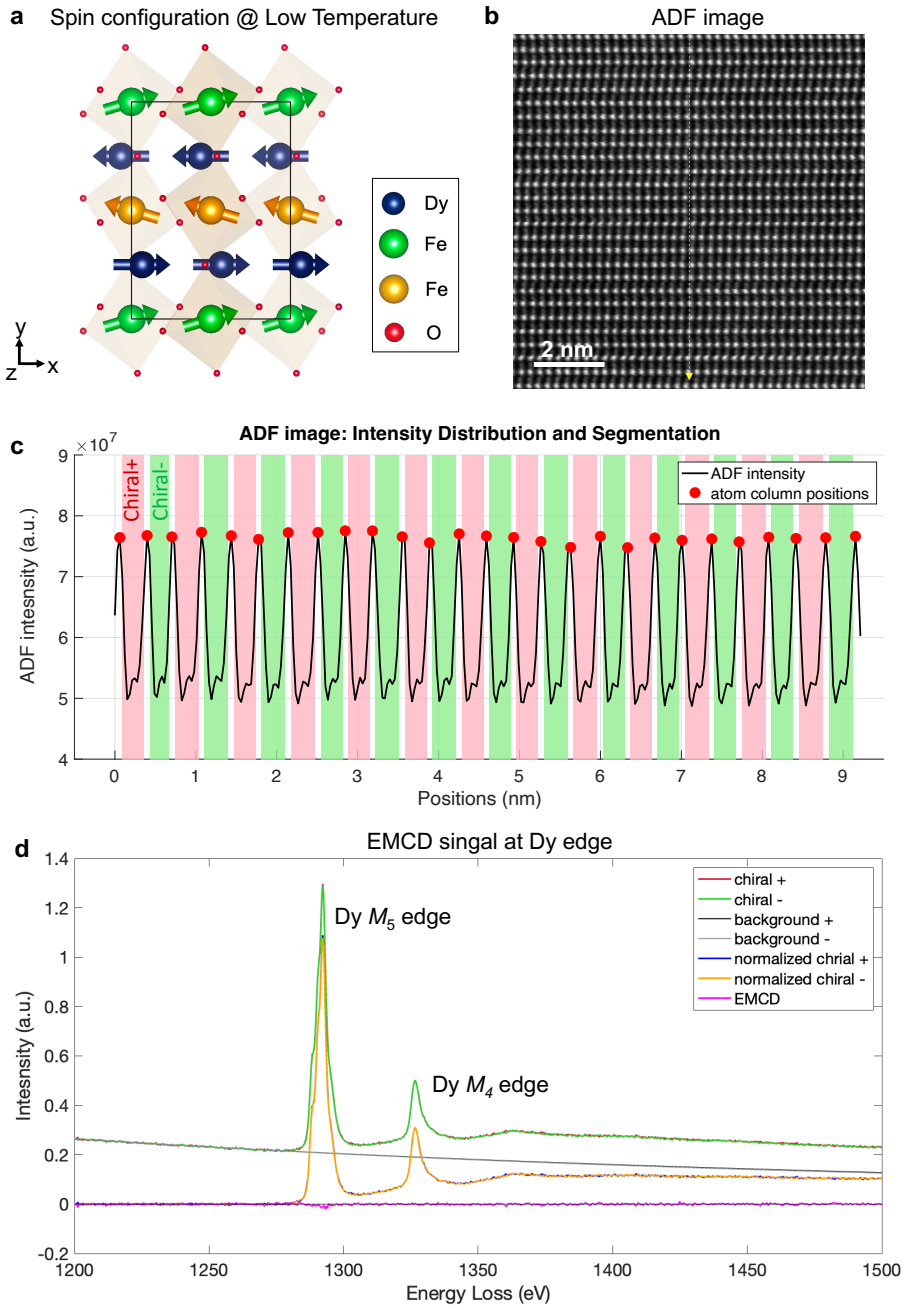


**Fig. S4 | EMCD signals for Dy in $DyFeO_3$. a**, Atomic model showing the spin configuration of $DyFeO_3$ below the Dy magnetic ordering temperature. **b**, ADF image of $DyFeO_3$ from the same STEM-EELS dataset as in **Fig. 2**. **c**, Line intensity profiles extracted from the ADF image in **b**, with the *chiral+* and *chiral-* regions indicated by red and green rectangles, respectively. **d**, Summed chiral EELS spectra from the *chiral+* and *chiral-* regions, along with their difference.

## Supplementary Note 5: EMCD spectra across the $DyScO_3$-$SmFeO_3$ interface

Atomic-column resolved EMCD spectra across the $DyScO_3$–$SmFeO_3$ interface are shown in **Fig. S5**, with the layer numbers indicated in Fig. 4 of the main text. The EMCD spectra for each layer are plotted together.

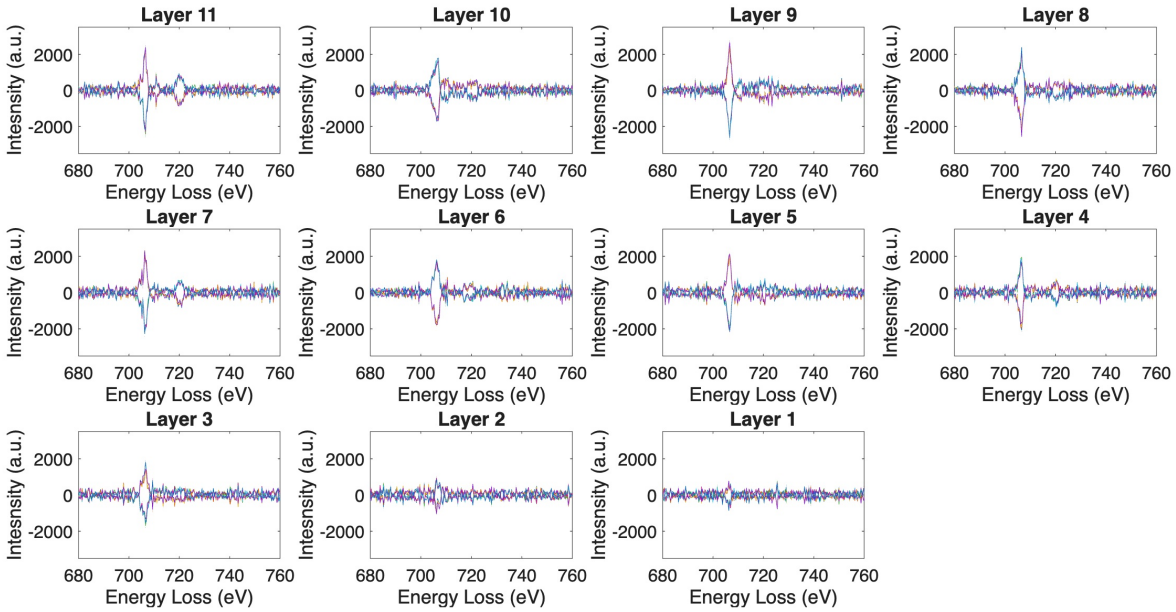


**Fig. S5 | Extracted EMCD signals for each atomic column at different layers across the interface.** The layer numbers are labelled in Fig. 4. The EMCD signals from columns 1 to 8 at each layer are plotted in the same panel.

## Supplementary Note 6: Dose dependence of EMCD signals

To minimize electron beam damage and sample drift, short acquisition times were used for each EELS spectrum over a large area during the STEM–EELS experiments. Based on the typical experimental parameters (beam current: 60 pA, pixel size: 0.325 Å, pixel dwell time: 3 ms), the electron dose for the $DyFeO_3$ measurements is estimated to be approximately $1.06 \times 10^7$ $e^-/Å^2$. However, this dose is insufficient to obtain reliable EMCD signals with a high SNR. In order to improve the SNR, a template matching method was applied. An analysis of the SNR of the EMCD signals with respect to the region size used for template matching is shown in **Fig. S6**. The SNR, which is defined as the ratio of the averaged Fe $L_3$-edge intensity to the standard deviation in the post-edge region (750 - 800 eV), is plotted in **Fig. S6a-c** as a function of the number of templates or integrated area. Representative EELS and EMCD signals are presented in **Fig. S6d-i**. It is evident that an SNR greater than 3 is achieved when 150 templates (corresponding to an integrated area of 5.2 nm × 5.2 nm) are used, enabling the reliable detection of EMCD signals (**Fig. S6e**). Accordingly, the effective electron dose required for atomic-scale EMCD measurement in $DyFeO_3$ is approximately $1.6 \times 10^9$ $e^-/Å^2$. The required region size could be further reduced by increasing the beam current and pixel dwell time, provided that the sample damage threshold allows it. We have also estimated the effective electron dose for $Fe_2O_3$ (Fig. 3). With the experimental parameters (beam current: 30 pA, pixel size: 0.325 Å, pixel dwell time: 1 ms), the estimated effective electron dose is approximately $1.8 \times 10^8$ $e^-/Å^2$ (corresponding to an integrated area of 2 nm × 2 nm), which is nearly an order of magnitude lower than that for $DyFeO_3$.

With regard to the comparison with electron ptychography, a much lower electron dose of $9.0 \times 10^5$ $e^-/Å^2$ was used[4]. The difference arises because electron ptychography is inherently dose-efficient. However, it requires extremely high phase precision to separate the weak magnetic signal from the dominant electrostatic contribution. In contrast, EMCD relies on the use of inelastically scattered electrons, for which the signal intensity decreases exponentially with increasing energy loss.

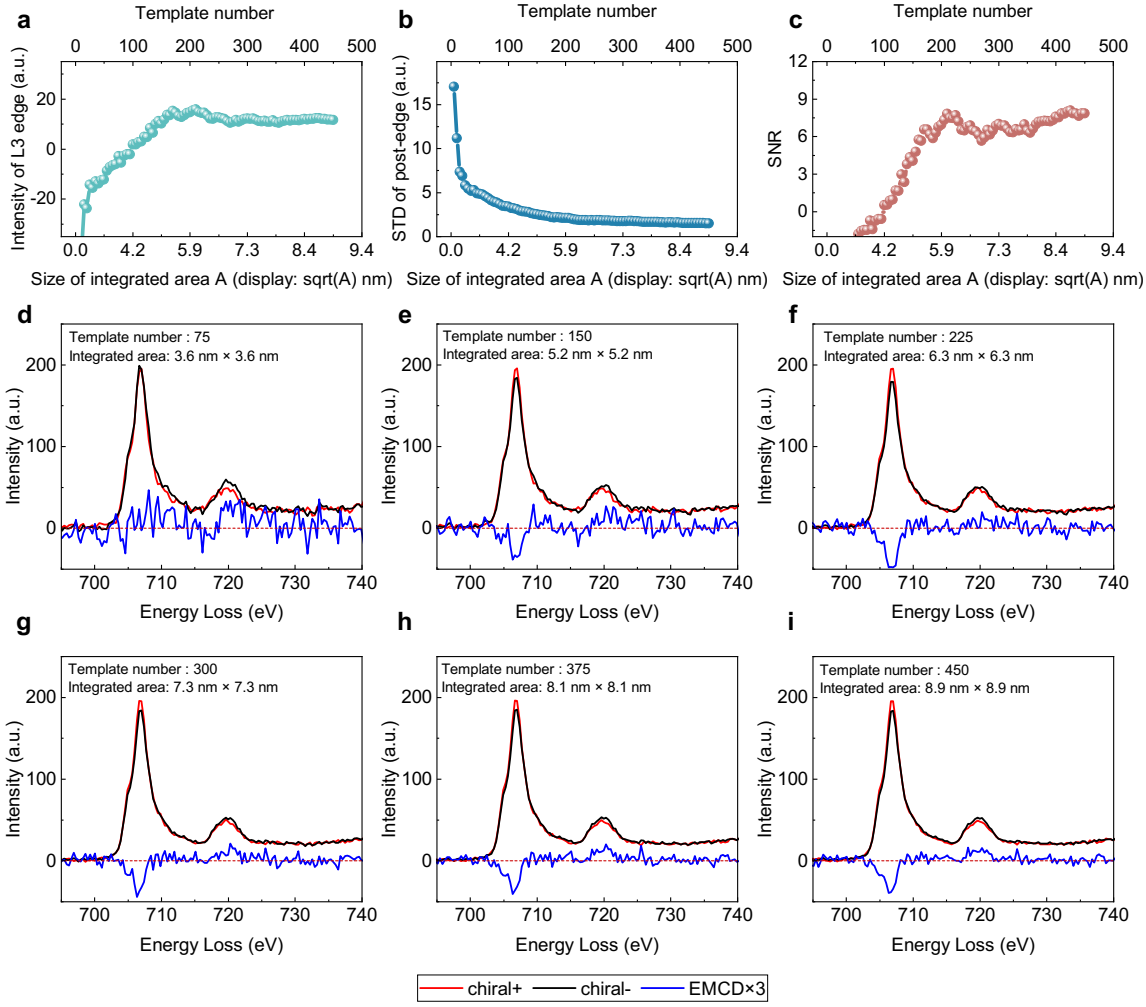


**Fig. S6 | Dose dependence of EMCD signals. a,** Average Fe $L_3$ edge intensity plotted *versus* template number and integrated area. The integrated area $A$ is plotted as $\sqrt{A}$ on the $x$-axis. **b,** Standard deviation (STD) of the EMCD signal intensity in the post-edge region (750-800 eV) plotted *versus* template number and integrated area. **c,** Signal-to-noise ratio (SNR) plotted as a function of template number and integrated area. **d-i,** Representative chiral EELS and corresponding EMCD difference signals at template numbers 75, 150, 225, 300, 375 and 450, corresponding to electron doses of $8 \times 10^8$ e$^-$/Å$^2$, $1.6 \times 10^9$ e$^-$/Å$^2$, $2.4 \times 10^9$ e$^-$/Å$^2$, $3.2 \times 10^9$ e$^-$/Å$^2$, $4.0 \times 10^9$ e$^-$/Å$^2$ and $4.8 \times 10^9$ e$^-$/Å$^2$, respectively.

## Supplementary Note 7: Effect of beam misorientation on EMCD signals

In conventional two-beam or three-beam EMCD setups, it is well established that the diffraction conditions strongly influence the distribution of magnetic signals in the diffraction plane, affecting both signal acquisition and reliable extraction. Therefore, it is important to evaluate how beam misorientation impacts real-space EMCD maps in the zone-axis geometry. In order to investigate this question, we performed simulations for $DyFeO_3$ with controlled beam tilts ranging from 0 to 5 mrad. This angular range can be routinely achieved in experiments using PACBED patterns. For simplicity, the tilt was applied independently along the *x*- and *y*-axes.

**Fig. S7a-c** shows real-space EMCD maps for tilt angles of $X$ = 0, 3 and 5 mrad, while **Fig. S7d-f** shows corresponding results for $Y$ = 0, 3 and 5 mrad. As the beam misorientation increases, the spatial distribution of the EMCD signals in real space remains nearly unchanged, with only a slight reduction in overall intensity observed for tilts up to 5 mrad. The integrated EMCD signal within the region marked by the red rectangle in **Fig. S7a** is plotted as a function of tilt angle, showing minimal variation within this range. However, when the tilt exceeds approximately 7 mrad, the simulations reveal a more pronounced degradation in signal strength. These results demonstrate that the zone-axis EMCD geometry is robust against beam misorientation, maintaining stable signal strength and spatial distribution for tilt variations up to 5 mrad in $DyFeO_3$. This tolerance is significantly broader than that for the conventional three-beam configuration, which typically requires sub-milliradian alignment to preserve signal integrity. This robustness arises from the high symmetry of the zone-axis geometry and from the use of an *on-axis* aperture, which compensates for asymmetries in the signal distribution in the diffraction plane.

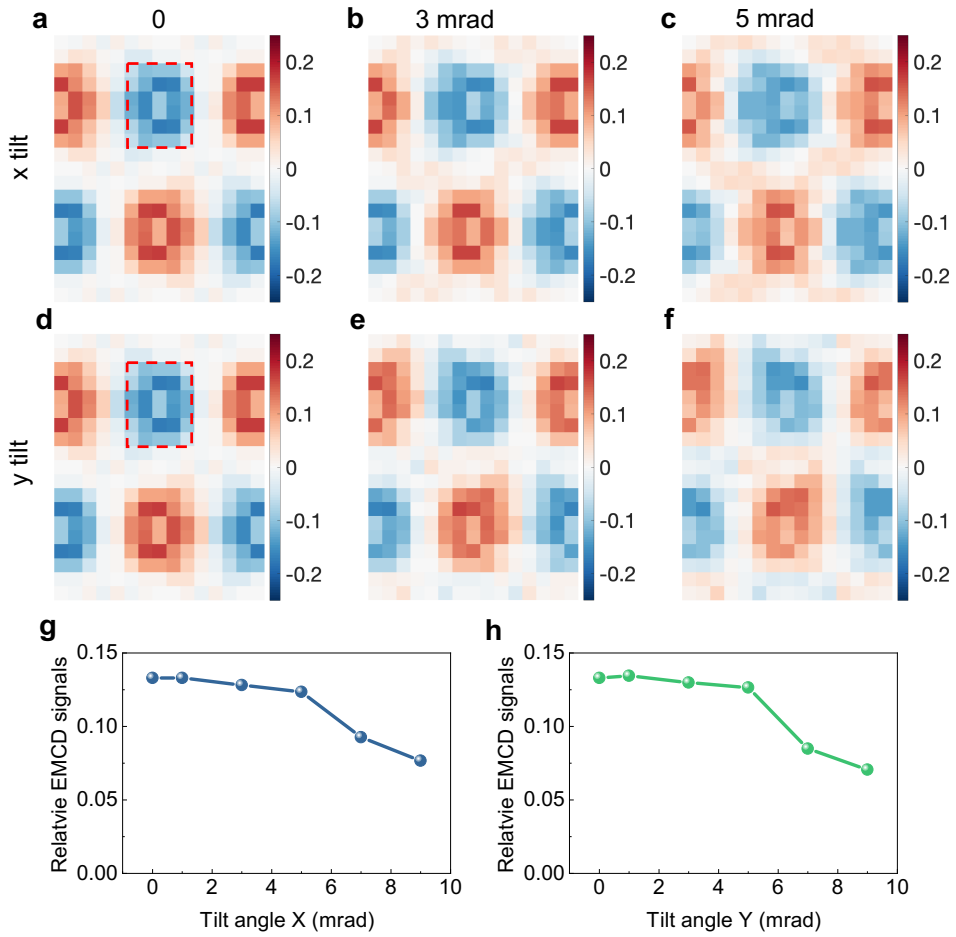


**Fig. S7 | Effect of beam tilt on EMCD signals in $DyFeO_3$. a-c**, Simulated real-space EMCD maps for beam tilts of $X = 0$, 3, and 5 mrad. **d-f**, Simulated real-space EMCD maps for beam tilts of $Y = 0$, 3, and 5 mrad. **g, h**, Integrated EMCD intensity in the region marked by the red rectangle in **a** and **d**, plotted as a function of the $X$- and $Y$-tilt angles, respectively.

## Supplementary Note 8: Simulation of the effect of a half–unit-cell offset shift on EMCD map measurement in $DyFeO_3$

In order to exclude the possibility of artifacts arising from the presence of a half–unit-cell offset in $DyFeO_3$ during EMCD map extraction, as described in Extended Data Fig. 5, a simulation test was performed in which the total EELS signal maps were artificially shifted by half a unit cell and then realigned (**Fig. S8,** upper panel). The resulting subtracted maps retained clear atomic contrast and reproduced the expected antiferromagnetic ordering pattern, confirming that our data processing workflow does not introduce artifacts, which could mimic magnetic order. We also constructed two total EELS signal maps excluding the magnetic contribution (**Fig. S8**, lower panel). The corresponding EMCD difference map exhibits very weak signals, in stark contrast to the upper panel, in which the magnetic contribution is retained. The residual signals arise from minor misalignments between the two stacks shifted by half a unit cell. Importantly, the weak residual signals are localized at the Fe atomic columns and are different from the alternating contrast characteristic of antiferromagnetic ordering.

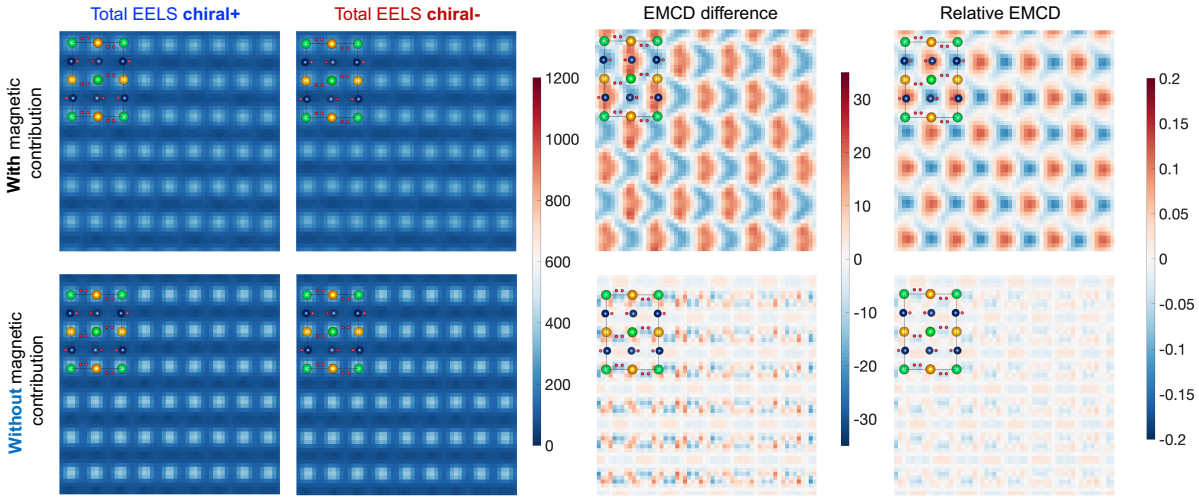


**Fig. S8 | Simulation test of the effect of a half–unit-cell offset shift on EMCD signal extraction.** Simulated total EELS signal maps for the *chiral+* and *chiral-* (shifted by half a unit cell with respect to *chiral+*) are shown in the left two columns. The corresponding EMCD difference and relative EMCD maps are shown in the right two columns. Upper panels: results obtained with the magnetic contribution, in which the EMCD maps preserve clear atomic magnetic contrast and reproduce the expected antiferromagnetic ordering pattern. Lower panels: results obtained without the magnetic contribution, showing very weak residual signals arising from minor misalignment between the two artificially-shifted stacks. The weak signals are localized at the Fe atomic columns (atomic model overlaid) and are clearly distinguishable from the alternating contrast characteristic of antiferromagnetic order.

## Supplementary Note 9: Alternative approach for the extraction of EMCD signals at the $SmFeO_3$-$DyScO_3$ interface

This alternative approach, which is described in the Methods section, is used to extract EMCD signals at the $SmFeO_3$–$DyScO_3$ interface. It avoids subtracting two chiral EELS stacks shifted by half a unit cell. The extracted EMCD maps, which are displayed in **Fig. S9**, are consistent with the results shown in Fig. 4 of the main text, which used a half-unit-cell shift.

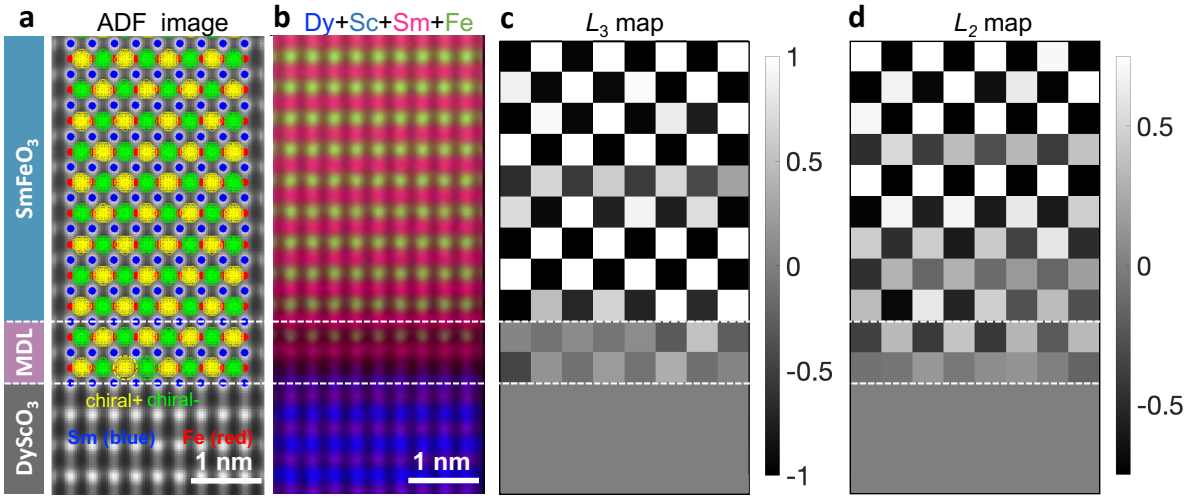


**Fig. S9 | Extraction of EMCD signals at the $SmFeO_3$-$DyScO_3$ interface without applying the half-unit-cell shift described in Extended Data Fig. 5. a,** ADF image across the interface after template matching. Sm (blue) and Fe (red) atomic columns are marked using corresponding colored dots. The chiral+ and chiral- regions used for chiral EELS signal extraction are indicated by yellow and green circles, respectively. **b,** Combined elemental maps for Dy (blue), Sc (violet), Sm (pink) and Fe (green) across the interface. **c,d,** EMCD maps at the $L_3$ and $L_2$ edges obtained by comparing the chiral EELS signals with the mean Fe $L$-edge spectrum.

**References**


1. Song, D. & Dunin-Borkowski, R. E. Three-Dimensional Measurement of Magnetic Moment Vectors Using Electron Magnetic Chiral Dichroism at Atomic Scale. *Phys. Rev. Lett.* **127**, 087202 (2021).
2. Song, D. *et al.* An in-plane magnetic chiral dichroism approach for measurement of intrinsic magnetic signals using transmitted electrons. *Nat Commun* **8**, 15348 (2017).
3. Rusz, J., Rubino, S., Eriksson, O., Oppeneer, P. M. & Leifer, K. Local electronic structure information contained in energy-filtered diffraction patterns. *Phys. Rev. B* **84**, 064444 (2011).
4. Cui, J., Sha, H., Yang, W. & Yu, R. Antiferromagnetic imaging via ptychographic phase retrieval. *Science Bulletin* **69**, 466–472 (2024).